Effective repeatable mechanoluminescence in heterostructured $Li_{1-x}Na_xNbO_3$: Pr^{3+}

Xiuxia Yang, Rong Liu, Xuhui Xu, Zhichao Liu, Mingzi Sun, Wei Yan, Dengfeng Peng, Chao-Nan Xu, Bolong Huang, Dong Tu**

X. Yang, Prof. D. Tu
School of Physics and Technology,
Wuhan University, Wuhan 430072, China
Email: tu-dong@whu.edu.cn

Prof. R. Liu
School of Chemistry and Chemical Engineering,
Wuhan Textile University, Wuhan430074, China

Prof. X. Xu, Z. Liu
Faculty of Materials Science and Engineering,
Kunming University of Science and Technology, Kunming 650093, China

M. Sun, Prof. B. Huang
Department of Applied Biology and Chemical Technology,
The Hong Kong Polytechnic University, Hung Hom, Kowloon, Hong Kong SAR, China
Email: bhuang@polyu.edu.hk

Prof. W. Yan, Prof. D. Peng
College of Physics and Optoelectronic Engineering,
Shenzhen University, Shenzhen 518060, China

Prof. C. N. Xu
National Institute of Advanced Industrial Science and Technology (AIST), Saga 841-0052, Japan

Prof. D. Tu
Suzhou Institute of Wuhan University, Suzhou 215123, China
Email: tu-dong@whu.edu.cn

Keywords: Mechanoluminescence, Repeatable, Heterostructures, Self-recoverable, Trap-controllable

Mechanoluminescence (ML) is a striking optical phenomenon that is achieved through mechanical to optical energy conversion. Here, a series of $Li_{1-x}Na_xNbO_3$: Pr^{3+}(x=0, 0.2, 0.5, 0.8, 1.0) ML materials have been developed. In particular, the synthesized $Li_{0.5}Na_{0.5}NbO_3$: Pr^{3+} relies on the formation of heterostructures, which is effectively coupling with the trap structures and piezoelectric property and to realize the highly repeatable ML performance without traditional pre-irradiation process. Furthermore, the ML performances measured under sunlight

irradiation and pre-heating confirm that the ML properties of $Li_{0.5}Na_{0.5}NbO_3$: Pr^{3+} can be ascribed to the dual modes of luminescence mechanism, including both trap-controllable and self-recoverable modes. In addition, DFT calculations further confirm that the doping of Na^+ ions in $LiNbO_3$ leads to electronic modulations by the formation of the heterostructures, which optimizes the trap distributions and concentrations. These modulations improve the electron transfer efficiency to promote ML performances. This work has supplied significant references for future design and synthesis of efficient ML materials for broad applications.

1. Introduction

Mechanoluminescence (ML) is the phenomenon of photon emission produced by certain materials under mechanical stimulus that has attracted intense attention in widespread applications including E-signature systems, artificial skins, light-emitting fabric, information storage, anti-counterfeiting, and optical imaging.[1-6] ML can be observed from materials during exposures to friction, impact, compression, stretching, bending, twisting, grinding, etc.[7,8] Thus, increasing interest has been attracted to ML research by many groups around the world. According to the recovery performance of ML, it is generally believed that ML materials can be divided into trap-controllable and self-recoverable two modes.[9,10] The trap-controllable ML is associated with the captured carriers in shallow and deep traps at around below the conduction band or above the valence band. It is relied on the induced energy releasing for the captured carriers from the traps, and it occurs for a certain level of mechanical stress (or strain) energy which is sufficient to activate the captured carriers releasing from the traps to recombine with emission centers, resulting in the ML phenomenon after removal the excitation source.[11,12] Self-recoverable ML materials are a special kind of luminescent materials, whose ML intensity can be output stable optical signals under the consecutive compressing-releasing cycles, and do not require light excitation to charge carriers.[13,14] Previous studies have shown that the self-recoverable ML materials depend on the generation of local piezoelectric fields, which

promotes the process of electron-hole recombination and realizes the self-recoverable ML process.[15-18] However, either trap-controllable or self-recoverable ML still leads to some shortcomings. Trap-controllable mode is the current mainstream way to achieve ML, but its pre-irradiation process and relatively poor repeatability seriously affect the performance and accuracy of stress sensing. Self-recoverable mode can be considered as a new type of ML, which exhibits better repeatability and need no pre-irradiation process. However, there are only a few kinds of self-recoverable materials (such as ZnS: Mn^{2+}, ZnS: Cu) that have been developed, and these materials mainly exhibit a kind of triboluminescence characteristics,[19,20] which is different from the more practical elastico-ML luminescence, because they only realize the stress sensing at the linear level, which is inadequate for 2D or even 3D stress sensing.[21,22] Meanwhile, it is worth noting that due to the coexistence of multiple factors in an ML process, the ML mechanism still has many disputes. Therefore, the ML mechanism analysis and the development of excellent ML materials performance are still urgent tasks.

Recently, the ML properties of many piezoelectric materials have been widely reported. For example, a series of Pr^{3+} doped recoverable ML materials with piezoelectric hosts calcium niobates composed of $mCaO{\cdot}Nb_2O_5$: Pr^{3+} (m = 1, 2, and 3) have been investigated by Zhang et al. [23] Tu et al. have reported that a sensitive red-emitting piezoluminescence material of $LiNbO_3$: Pr^{3+} by manipulated Li/Nb ratio.[24] Moreover, a ferroelectric material $Sr_3Sn_2O_7$: Nd^{3+} with ultrasensitive and sustainable near-infrared piezoluminescence has been explored by Tu et al..[25] However, all the above-mentioned materials need to be pre-irradiated by UV light to achieve excellent ML properties, indicating that they can be classified as trap-controllable ML materials. In fact, the electrons stored in the traps after excitation are the key to the trap-controllable ML, which is in close correspondence with long persistent luminescence (LPL). In previous reports, some LPL materials can be effectively excited by sunlight,[26-28] however, ML

materials that can be excited by sunlight are rarely reported. Meanwhile, the ML materials can be activated by sunlight, indicating that the effective absorption and storage of the solar energy in traps, which can further convert into light emission under the mechanical stimulus. It will greatly reduce energy loss and facilitate the repeatable process of ML. This kind of material can make sufficient use of solar energy as well as reduce energy consumption significantly. On the other hand, ML materials by self-recoverable mode recently have received wide attention, such as ZnS: Cu. Jeong et al. have explored the ML performance of ZnS: Cu film, which has realized a reproducible intensity for over 100000 cycles under repeated stretching.[20] Wang et al. have reported that the ZnS: Mn^{2+} film showed stable ML intensity under repeated compression tests. The above self-recoverable ML materials show good ML repeatability and need no pre-irradiation process, but their mechanisms are still unclear.[19] In particular, whether the residual carriers captured lattice defects affect the ML repeatability is a key problem. As widely known, the pre-heating method is an effective way to empty the residual carriers. Thus, we have combined the pre-heating method with the ML analysis can eliminate the influence factors of residual carriers, and realize the accurate analysis of the ML mechanism.

In this work, we have successfully constructed the heterostructures by doping Na^{+} ions in $LiNbO_3$ and synthesized a series of ML materials. In particular, the ML material of $Li_{0.5}Na_{0.5}NbO_3$: Pr^{3+} relied on the coupling of the trap structures and piezoelectric property, which can be activated by sunlight to achieve repeatable ML performance. The repeatable ML performance is realized by sunlight excitation due to the capture of charge carriers are captured in traps. These trapped carriers are released from traps to recombine with emission centers under the mechanical stimulus. Furthermore, to confirm the true source of ML in $Li_{1-x}Na_xNbO_3$: Pr^{3+}, we have adopted the pre-heating method to release the captured carriers from trap structures before ML measurement. Meanwhile, DFT calculations have revealed that the formation of heterostructures in $Li_{0.5}Na_{0.5}NbO_3$ evidently affects the electronic structures. With

the Na doping, the trap distribution and concentrations become broader and higher, supporting the remarkable ML performances. This work has supplied novel and promising strategies to improve ML performances in future works.

2. Results and discussion

Figure 1a shows the XRD patterns of $Li_{0.5}Na_{0.5}NbO_3$: Pr^{3+} (LN0.5) sample. All the diffraction peaks are exclusively well assigned to either trigonal phase *R3c*-$LiNbO_3$ (JCPDS No. 20-0631) or rhombohedral phase *R3c*-$NaNbO_3$ (ICSD No. 9013407), indicating the formation of LN0.5 composition. The Rietveld refinement result of the LN0.5 is shown in Figure 1b. The black crosses and red solid lines are raw and calculated patterns, respectively. The green and violet short vertical lines show the position of the Bragg reflections of the calculated pattern of *R3c*-$NaNbO_3$ and *R3c*-$LiNbO_3$, respectively. The difference between the raw and calculated patterns is plotted using the blue line at the bottom. The reliability parameters of refinement are R_{wp}=11.21%, R_p=8.19%, and χ^2=4.3, which demonstrates that the refined results are reliable and the crystal structure is confirmed to *R3c*-$LiNbO_3$ and *R3c*-$NaNbO_3$. A series of XRD patterns of LNx are shown in Figure S1, which shows that the rhombohedral phase structure of $NaNbO_3$ gradually occupies a larger proportion with the increase of Na/Li ratio, and when x=1.0, it is completely converted to the orthorhombic phase of $NaNbO_3$. It shows that sodium niobate has a rich phase transition process in the system of LNx. Figure 1c-e illustrates the crystal structure of *R3c*-$LiNbO_3$, *R3c*-$NaNbO_3$, and *Pbma*-$NaNbO_3$, respectively.[29-31] As shown in Figure 1c, the crystal structure of $LiNbO_3$, each Nb^{5+} ion is surrounded by six O^{2-} ions, forming twisted oxygen octahedra, and these [NbO_6] octahedra are linked by sharing common oxygen atoms. Figure 1d exhibits the perovskite crystal structure of $NaNbO_3$, crystallizing in a rhombohedral phase. It has a much higher degree of distortion than the structure of $NaNbO_3$ in the orthorhombic phase. Figure 1e illustrates the $NaNbO_3$ crystal structure of the orthorhombic phase. The crystal structure consists of two types of Na sites and a [NbO_6] octahedral. The

sodium occupies interstitial sites located in the unit cell vertex, and niobium occupies the octahedral site.

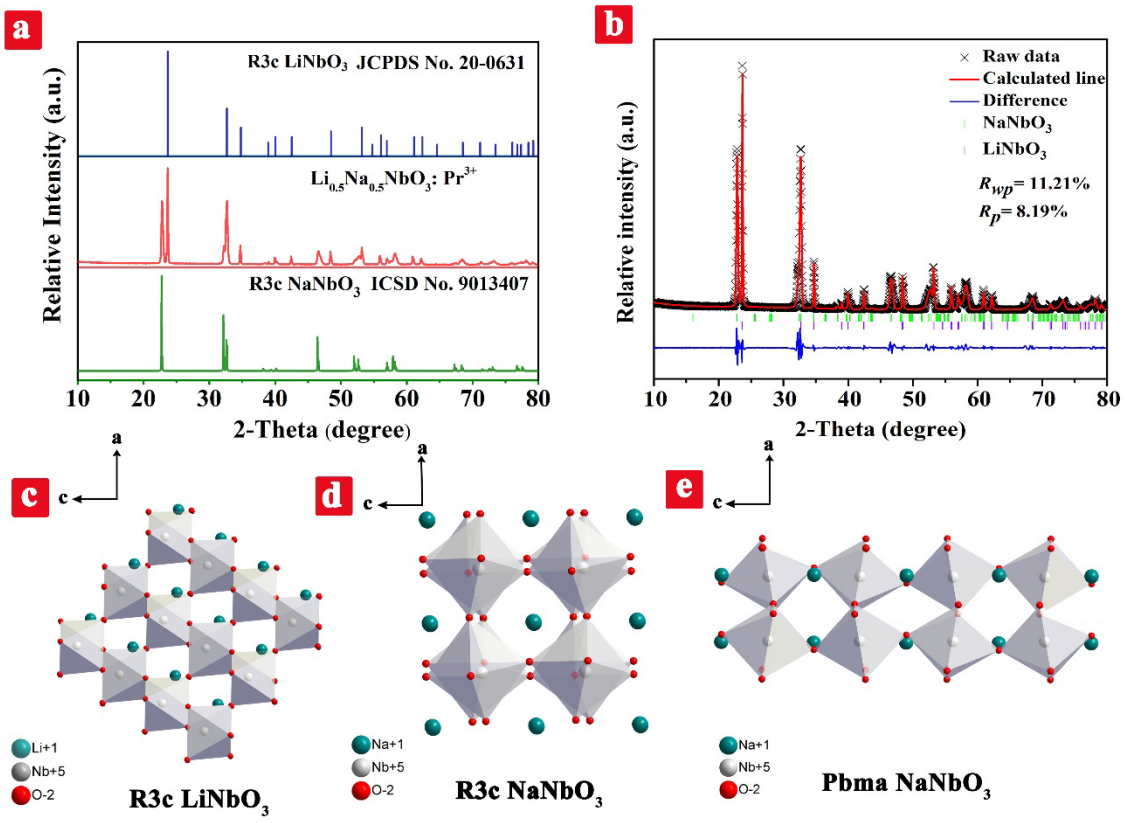

Figure 1. The XRD patterns of LN0.5, the standard card of JCPDS No. 20-0631 and the ICSD No. 9013407, respectively (a); XRD refinement results of LN0.5 (b); Crystal structure of $LiNbO_3$ (c) and $NaNbO_3$ (d, e), respectively.

To explore the delicate chemical microenvironment changes in the samples, XPS spectra of LNx are employed, as shown in **Figure 2** and Figure S2, respectively. Figure 2a depicts the XPS spectrum of LNNOP, the peaks corresponding to Na(1s), Pr(3d), O(1s), C(1s), Nb(3d), Nb(1s), and Li(1s) can be clearly detected. Figure S2 compares the XPS spectra change of LNx. It can be seen that as the ratio of Na/Li increases, the corresponding position of the binding energy spectrum shifts. Figure 2b illustrates the high resolution XPS spectrum of Pr(3d) consists of $3d_{3/2}$ and $3d_{5/2}$ peaks, confirming that the Pr^{3+} ions are successfully doped in $Li_{0.5}Na_{0.5}NbO_3$ compound. It matches well with the formerly reported XPS features in the $LaMnO_3$: Pr^{3+}sample and $LiNbO_3$: Pr^{3+}. [32,33] Figure 2c and Figure S2(f-j) demonstrate the high resolution XPS

spectra changed of Li(1s)-Nb(4s) with different ratios of Na/Li. The Li(1s)-Nb(4s) peak intensities are fitted after nonlinear background subtraction (Iterated Shirley), as depicted in Figure S2(f-j). It can be obviously seen that the peak position of Li(1s)-Nb(4s) has changed significantly with the ratio of Na/Li increases. Through Gaussian fitting, there are three peaks in the high resolution XPS spectra of Li(1s)-Nb(4s), which are divided into peak1 (Nb 4s 62.2 eV), peak2 (Nb 4s 59.6 eV) and peak3 (Li 1s 55 eV), respectively.[34] As the ratio of Na/Li ratio increases, peak1 gradually increases and then becomes stable, peak2 gradually decreases and maintains stable, and peak3 gradually disappears. Notably, the chemical binding energy difference is contributed by the Fermi level shift, which is the evidence that the doped Na^+ ions make the crystal field environment change. The subsequent DFT calculation results will further prove that the phenomenon is caused by the band offset with heterostructures.

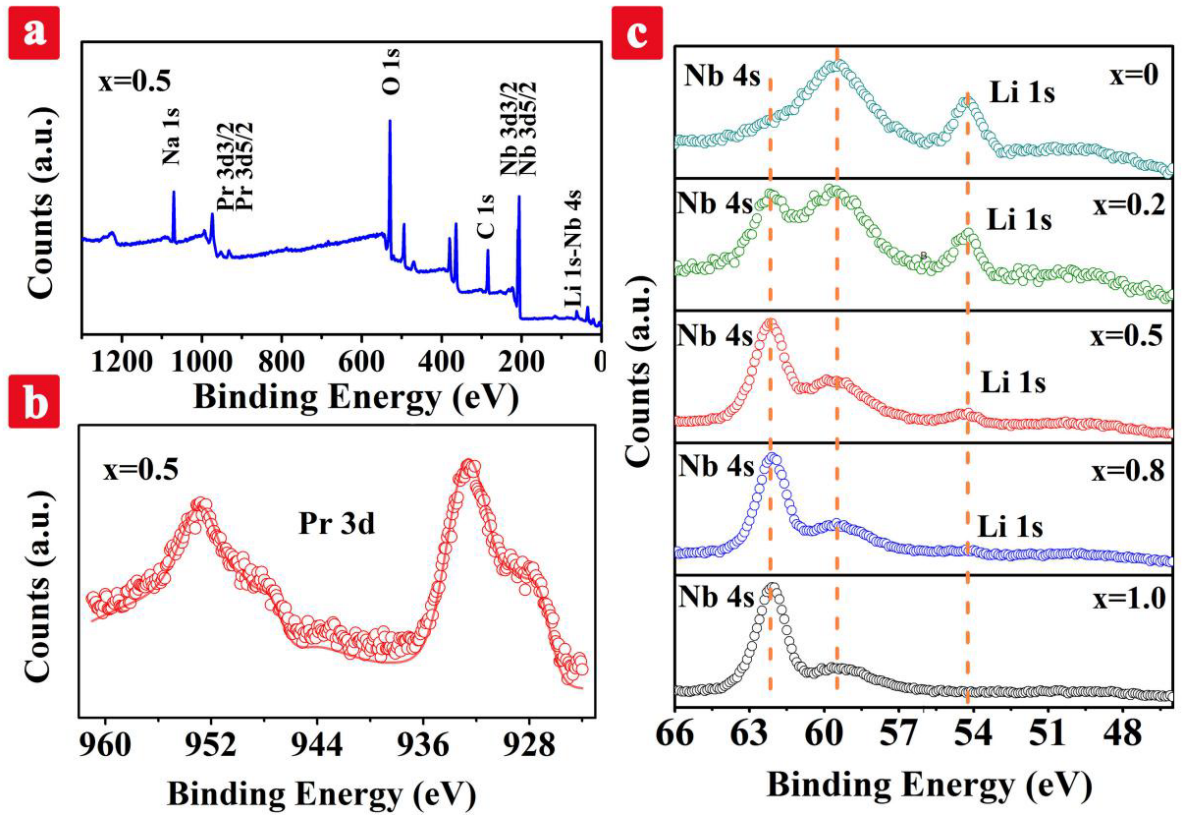

Figure 2. XPS spectrum of LN0.5 (a) and (b) the high resolution XPS spectrum of Pr(3d); The Li(1s)-Nb(4s) high resolution XPS spectra of LNx, respectively (c).

PL, PLE and absorption spectra of LN0.5 are recorded at room temperature, as displayed in **Figure 3a**. The PL spectrum shows the characteristic emission bands of Pr^{3+} ions with a maximum intensity at 613 nm under the excitation of 302 nm. The dominant red emission is attributed to the $^1D_2 \rightarrow {}^3H_4$ transition of Pr^{3+} ions. The absorption spectrum exhibits well consistent with the PLE spectrum. When monitored at 613 nm, the excitation bands centered at 302 nm and a broad band at 440-500 nm are presented, respectively. The peak center at 302 nm can be ascribed to the absorption of $Li_{0.5}Na_{0.5}NbO_3$ host, and the band at 440-500 nm corresponds to the *f-f* transitions ($^3H_4 \rightarrow {}^3P_j$, j=0, 1 and 2) of Pr^{3+} ions. Figure 3b shows the position of emission peaks changed between LNx. When x=0, the dominant red emission (619, 637 nm) is attributed to the $^1D_2 \rightarrow {}^3H_4$ transition of Pr^{3+} ions. With the ratio changes, the position of the emission peak changes from 619 to 611 nm, and the red emission of 637 nm gradually disappeared. [5,24,35] The normalized PLE and PL spectra of LNx are shown in Figure S3 and Figure 3c, respectively. With the change of the Na/Li ratio, the excitation peak position of LN0.5 has changed significantly. It can be clearly seen that the PLE spectrum displayed a broad band with a peak at 345 nm and a band at 450-550 nm when x=0, and with Na^+ ions doped increasing the *f-f* transitions ($^3H_4 \rightarrow {}^3P_j$, j=0, 1 and 2) intensity of Pr^{3+} ions gradually decrease, and the host absorption gradually dominates. Meanwhile, as the ratio of Na/Li changes, the position of the excitation peak gradually moves to the ultraviolet region, as shown in Figure S3. Moreover, the emission peak position shifted from 619 nm to 611 nm, as shown in Figure 3c. These results further confirmed that the lattice environment of LN0.5 has undergone a greater change, with the doped of Na^+ ions content increasing, the internal electron distribution is disordered, thus the host absorption of LN0.5 increased and shifted, and the above content can be proved again by the measurements of fluorescence decay curves (Figure S4). Figure 3d shows the diffuse reflectance spectra of LNx, which displays the characteristic locations of the ultraviolet (UV) absorption edges in the LNx systems, indicating their difference in the optical bandgap. According to the Kubelka-Munk function and the Tauc relation,[36] the optical

bandgap of the samples is evaluated to be 3.02, 3.06, 3.26, 3.34, 3.36 eV, respectively, as shown in Figure 3e. Notably, it can be seen that the bandgap increases with rising the ratio of Na/Li.

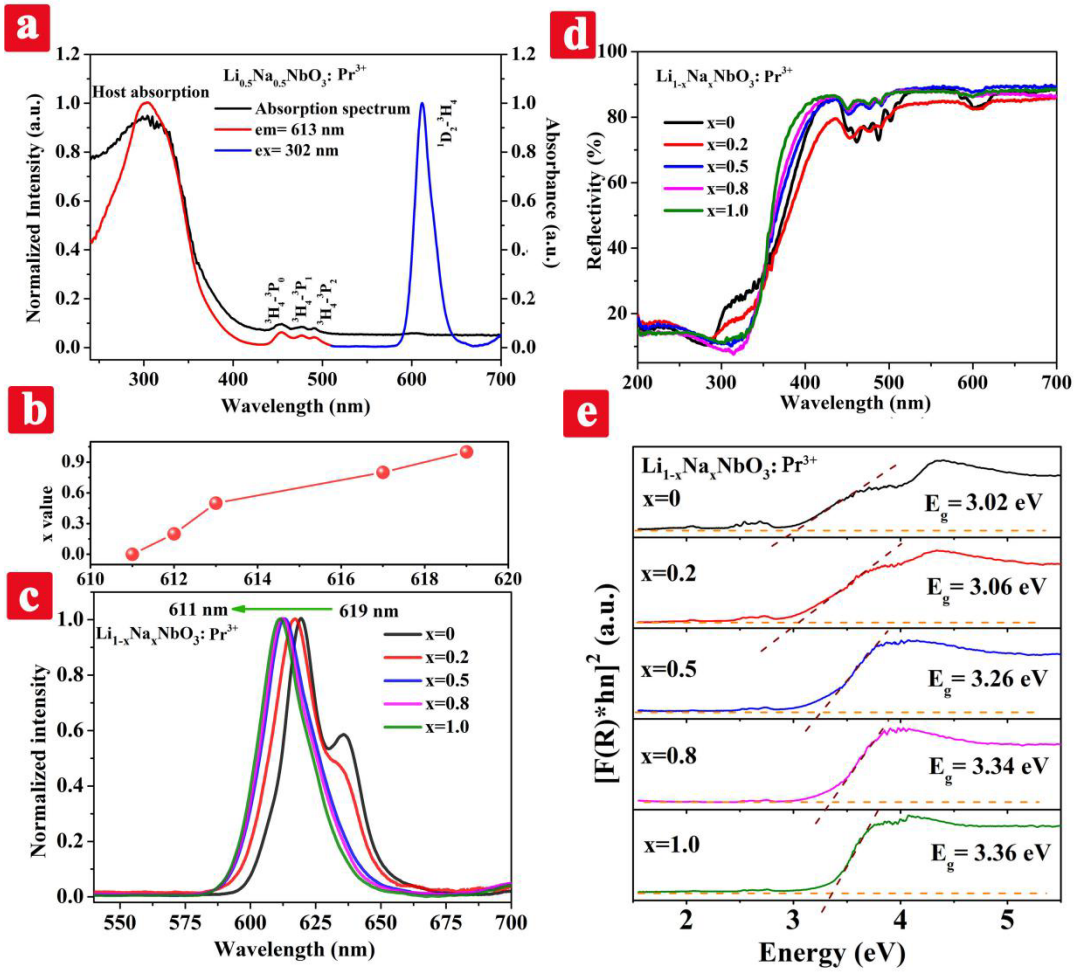

Figure 3. PL (λ_{ex}= 302 nm), PLE (λ_{em}= 613 nm) and absorption spectra of LN0.5 (a); Emission peak of LNx as a function of x value (b); Normalized PL spectra of LNNOxP (c); Diffuse reflection spectrum of as-synthesized LNNOxP (d); The estimated optical band gap of LNx (e).

To investigate the effect of increasing Na^+ ions on the ML properties of piezoelectric materials, the ML properties of LNx are recorded without any pre-irradiation conditions, as shown in Figure S5(a-e), it is unambiguously proved that the ML performance increased with the increase of Na^+ ions content, and reached the maximum when x=0.5. Figure S5f compares the ML responses of LNx. It can be obviously observed that the optimal ML response is obtained when x=0.5. Moreover, the PL and ML spectra of LN0.5 are shown in Figure S6. It can be seen that the ML and PL spectra exhibit the same red emission characteristic, suggesting the same

luminous center of Pr^{3+} ions ($^1D_2 \rightarrow {}^3H_4$). The ML intensity increased with the increasing of Na^+ ions concentrations and reached the maximum when x=0.5. It is consistent with the result of recoverable ML performance shown in Figure S5. **Figure 4a(i)** shows the image of the LN0.5 pellet before and during load for 1000 N using a test machine. As shown in Figure 4a(ii), the red ML is generated from the pellet during loading, it can be obviously observed that the red emission in the stress concentration area of the pellet, exhibiting a good visualization effect of stress. Figure 4b compares the experimental ML intensity with the simulated stress distribution along with Y'OY direction of the LN0.5 pellet under the load of 1000 N. In this image, y is the distance from the center O along with Y'OY direction, and R is the radius of the disc. The ML intensity (red dots) plotted versus y/R is consistent with the simulated load stress along the Y'OY direction (black line). These results demonstrate that the LN0.5 pellet can reflect well the stress distribution on a 2D plane against the axial stress, further indicating that the ML of LN0.5 can be ascribed to the elastico-ML characteristic which is different from the triboluminescence only at the friction position. Figure 4c depicts the ML response of LN0.5 under the compressive load. The peak intensity of ML has a significant decay under the consecutive compressing-releasing cycles. Figure 4d shows a representative triangular wave mode ML response of LN0.5 pellet under a compressing-releasing process, the ML intensity of LN0.5 gradually increased with the increase of compressive load and decreased sharply after releasing the load. Aiming at practical applications, the repeatability of the LN0.5 sample is carefully investigated, and presented in Figure 4e by applying a load of 1000 N by the test machine for more than 50 cycles. Although the ML intensity gradually decreased, the stable ML signals still can be detected in even more than 50 cycles. The inset demonstrates the real-time ML intensity during 90-135s (i) and 410-445s (ii). These results clearly indicated that the excellent ML repeatability of LN0.5 samples after repeated operations, which are promising candidates for making them reliable for practical applications.

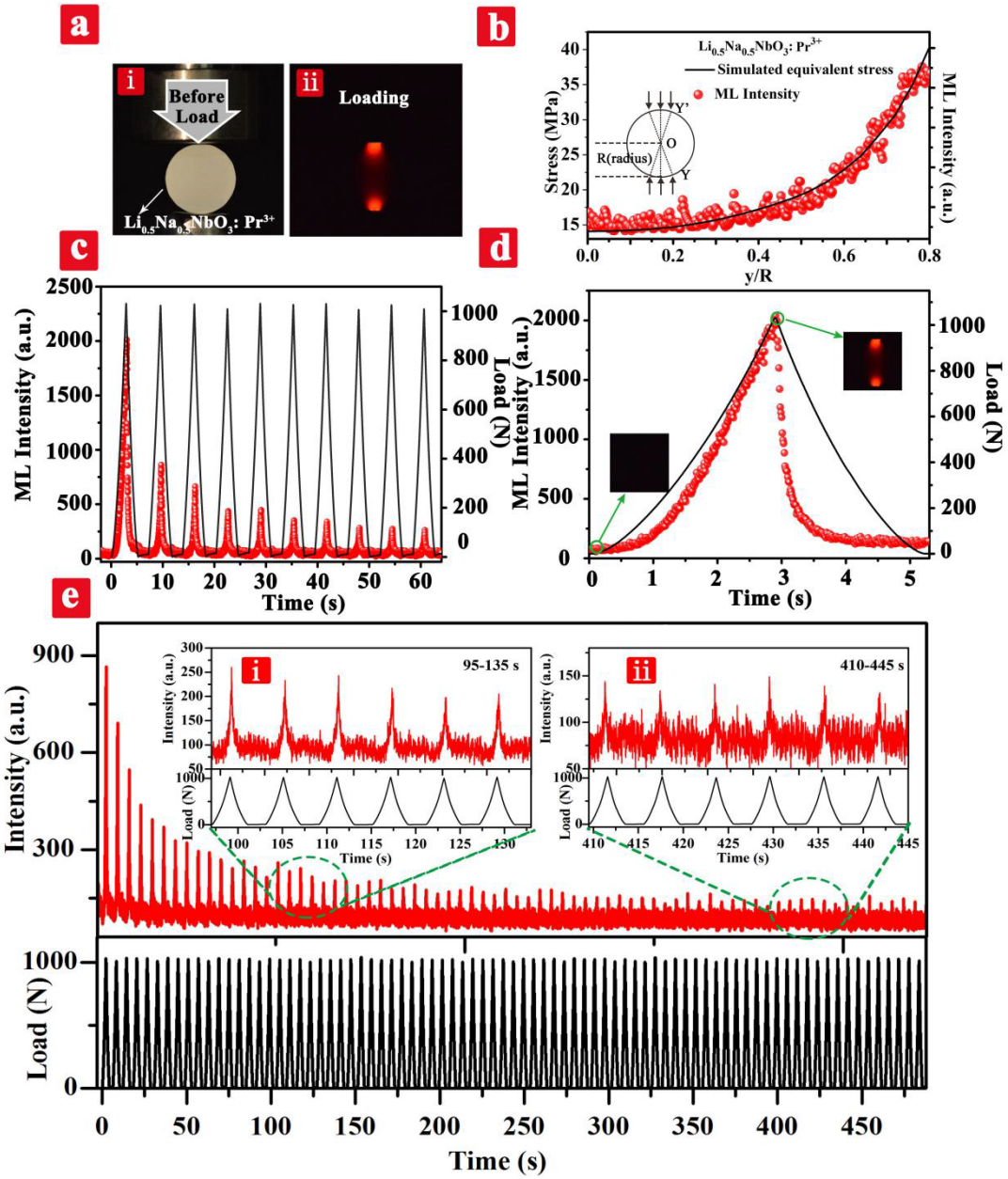

Figure 4. The image of the LN0.5 pellet before load (i) and loading (ii) (a); Comparison of experimental and simulated stress distribution along Y'OY of the LNNOP pellet under a compressive load of 1000 N, Inset: schematic of the sample (b); ML decay behavior of LN0.5 under the consecutive compressing-releasing for 10 cycles (c); ML response of LN0.5 pellet under loading applied in a triangular wave mode (d); Stability and repeatability test of LN0.5 pellet load more than 50 cycles: (i) the real-time ML intensity during 95-135 s; (ii) the real-time ML intensity during 410-445 s (e).

All the above samples are not deliberately to avoid light before tests, thus, to explore the ML mechanism in LNx, we use two methods of adjusting the sunlight irradiation time and pre-heating treatment to analyze the ML performance. As shown in **Figure 5a**, TL curves of LNx

samples are investigated under sunlight irradiation for 30 min. The maximum initial intensity is recorded in LN0.5. Figure 5b depicts the TL curves of LN0.5 under sunlight at 12 noon irradiation for 5 min, 30 min, 1 h, 3 h, 5 h, respectively. It can be obviously seen that with the irradiation time of sunlight increasing, the TL intensity of LN0.5 gradually increases, and the maximum value is obtained when irradiated for 1 h, and the TL peak gradually moves to the high temperature area. It can be attributed to the carriers in the shallow traps are gradually released with the exposure time increases. It should be noted that although we try to keep the samples exposed to the same weather, there will be some errors due to the large weather changes. Therefore, the following tests are uniformly selected under the conditions of sunlight irradiation for 30 min. Figure 5c compares the ML responses of LN0.5 under different sunlight irradiation time. It is noted that the ML response gradually increases and eventually maintains stability after irradiation 30 min. The result is almost consistent with the TL curves that we have recorded in Figure 5b. In addition, we also used UV light and blue LED to irradiate LN0.5 phosphor for the ML test, as exhibited in Figure S7. The results demonstrated that the phosphor has excellent recoverable ML properties regardless of the UV light or blue LED excitation conditions. Figure 5d shows the ML peaks intensity of continuous compression for 10 cycles, the peak intensity of ML has a significant decay under the consecutive compressing-releasing cycles. However, the attenuated ML intensity can be fully recovered after the sunlight irradiation, and the recoverable ML possesses a high reproducibility during the repeated loading sunlight irradiation cycles.

Although ML under sunlight irradiation shows better practical application, it is still based on the trap-controllable ML characteristics. In order to further explore the real physical effect of stress on ML from LN0.5, we have made a pre-heating treatment to carry out the following analysis. Through this method, the residual carriers captured by lattice defects can be emptied effectively, thus, the TL curves and ML intensity of LN0.5 are recorded after the pre-heating

treatment process. Considering the proper removing temperature of carriers from traps and the limited heat-resistance temperature of epoxy resin, we choose 100℃ for pre-heating. As depicted in Figure 5e, the TL curves of LN0.5 are recorded after sunlight irradiation for 30 min and heated at 60℃, 100℃ for 1 h. Initially, an obvious TL curve can be observed, after heating at 60℃ for 1 h, the TL intensity shows a sharp decline, indicating that the captured carriers have not been completely empty from traps. After heated at 100℃ for 1 h, the TL intensity completely disappears, which reveals the captured carriers are almost entirely released from traps. Subsequently, the ML intensity of LN0.5 heated at 100℃ for 1 h is measured, as shown in Figure 5f. It can be clearly seen that the ML signals are obviously detected even after the captured carriers are completely emptied. Moreover, under the continuous compression of 10 cycles, the peak intensity of ML shows almost no attenuation and remains the initial intensity. The results reflect that the ML from LN0.5 is not entirely attributed to the trap-controllable mode. Even in the case after the pre-heating treatment and the captured carriers are almost removed, an effective and repeatable ML still can be detected, which indicates that the ML properties from LN0.5 can be ascribed to not only the trap-controllable mode but also self-recoverable mode. Unlike the previously reported self-recoverable materials, the material of LN0.5 uses pre-heating to remove the stored charge carriers in the traps, successfully achieving a repeatable mechanical to optical energy conversion. In particular, previous studies demonstrate that the phosphors of LN0.5 possessed piezoelectric crystal structures.[29] Therefore, combined with the piezoelectricity of the material, we believe that the applied stress can lead to the piezoelectric field, which causes the phenomenon of light emission under compressive load.[37,38] The possible trap-controllable and self-recoverable mode ML processes of LN0.5: Pr^{3+} materials are schematically illustrated in Figure S8. As shown in Figure S8a, under the excitation of sunlight at ambient temperature, the electrons act as carriers are promoted to the conduction band (process ① in Figure S8a), and then captured by the traps

below the conduction band (process ②). Under the compressive load in the darkroom, the local piezoelectric field is triggered, causing the carriers released to the conduction band from the traps, then gradually back to the excited levels of Pr^{3+} ions through conduction band during the stimulus of mechanical stimulation (process ③), and these electrons recombined with emitting centers to generate bright red emission (process ④). After heated at 100℃ for 1 h, the self-recoverable mode of the ML mechanism has been proposed in Figure S8b. In the compressive loading process, a local piezoelectric field is generated, resulting in the piezoelectric polarization charges and the separation of the electron-hole pair. Subsequently, the partial electrons and holes can break free from the restraint, that is, the electrons are promoted to the conduction band, and the holes enter the valence band (process ① in Figure S8b). Finally, the de-trapped electrons and holes recombine by transferring energy to the Pr^{3+} ion, resulting in red-emitted ML. (process ② and ③).

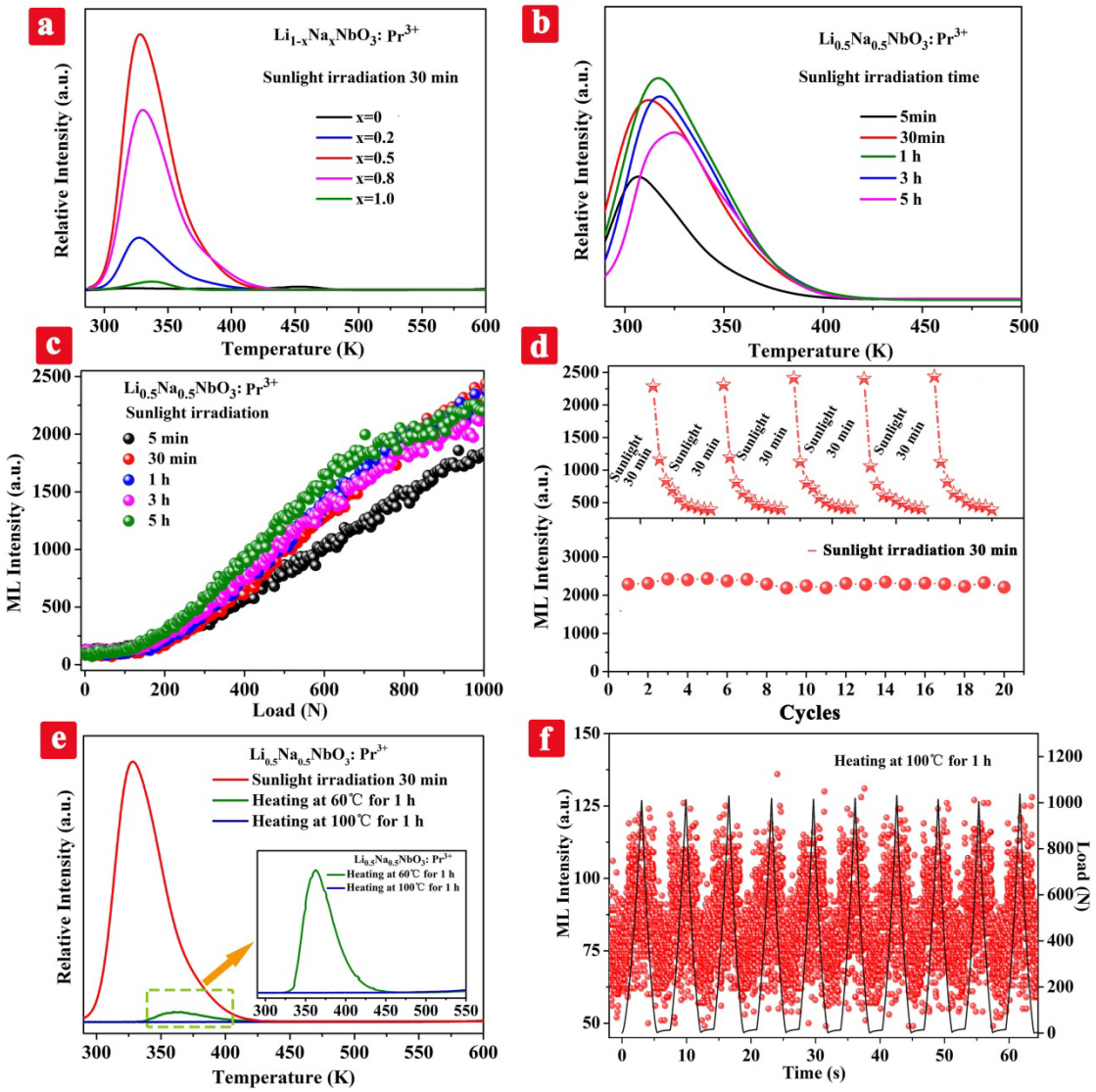

Figure 5. TL curves of LNx under sunlight irradiation for 30 min (a); TL curves of LN0.5 under sunlight irradiation for 5 min, 30 min, 1 h, 3 h, 5 h, respectively (b); Comparison of ML intensities for LN0.5 with different irradiation time (c); ML recovery behavior and reproducibility of LN0.5 after sunlight irradiation 30 min (d); TL curves of LN0.5 under sunlight irradiation for 30 min and heated at 60 ℃, 100 ℃ for 1 h, respectively (e); ML decay behavior of LN0.5 under the consecutive compressing-releasing for 10 cycles after heated 100℃ for 1 h (f).

To further investigate the remarkable ML performances in LN0.5, we have carried out the DFT calculations. The electronic distributions near the Fermi level (E_F) have been demonstrated to indicate the influences induced by the Na^+ ions doping. As depicted in **Figure 6a**, it can be noted that $LiNbO_3$ has shown highly ordered electronic distributions, in which the O sites and Nb sites dominate the bonding and anti-bonding orbitals, respectively. With the high

concentration of Na^+ ions doping, we expect the formation of heterostructures to facilitate ML performance. Figure 6b and 6c exhibit the heterostructures in the xy axis (Hetero1) and z-axis (Hetero2). For Hetero1, although the dominant contributions of Nb sites remain, the orbital distributions near O sites are evidently disturbed. Meanwhile, for Hetero2, the bonding orbitals are mainly concentrated on the $NaNbO_3$ side while the $LiNbO_3$ side mostly shows the anti-bonding orbitals. When the Li^+ ions are completely replaced by the Na^+ ions, the electronic distributions become highly ordered again, which is similar to $LiNbO_3$, as shown in Figure 6d. These results support that the intrinsic electronic structures are affected by the Na^+ ions doping. Then, the detailed projected partial density (PDOS) of states is plotted, as exhibited in Figure 6e. For $LiNbO_3$: $0.01Pr^{3+}$, the O-s, p, and Nb-4d orbitals dominate the valence band maximum (VBM) and conduction band minimum (CBM). In comparison, the contributions of Li-2s orbitals are not evident. The dominant peak of Pr-4f orbitals locates in the mid-bandgap of the host material to activate the ML from the electron-hole recombination. Since the PDOS of Hetero1 and Hetero2 are similar, we only display Hetero1 as the representative. Although the overall PDOS does not significantly change, we still notice the upshifting of Nb-4d orbitals in CBM from E_V+2.0 eV in $LiNbO_3$ to E_V+2.6 eV in Hetero1, as demonstrated in Figure 6f. In comparison, the $NaNbO_3$: Pr^{3+} exhibits a distinct electronic structure. It can be clearly observed in Figure 6g, the contribution of Pr-4f in VBM is absent, which dominantly locate within the mid-gap. As a result of electronic modulation, the absorption spectra are also different. Notably, the absorption spectra of Hetero1 and Hetero2 are highly similar, which show the absorption peak at 230 and 270 nm, respectively. The absorption peaks of $LiNbO_3$ and $NaNbO_3$ have shifted towards the longer wavelength at 260 and 244 nm. However, the absorption intensity of both $LiNbO_3$ and $NaNbO_3$ are weaker than the heterostructures, supporting their superior ML performance of LNNOP, as shown in Figure 6h. To further understand the improved ML performances in the heterostructures interfaces, we demonstrated the band offset for different elements. For Li-2s, we observe the 0.35 and 0.18 eV upshifting of the gap states, which leads

to the increased concentration of deep traps, as shown in Figure 6i. For Na-3s orbitals, there are two gap states locate within the bandgap. For the interface of the heterostructure, such gap states merge into one brad peak and upshift around 0.37 and 0.62 eV. These results indicate that some shallow traps become deep traps due to the Na^+ ions doping, resulting in the broaden trap distributions to guarantee high ML performances, as depicted in Figure 6j. For the Nb-4d orbitals, the electronic modulations are revealed in the CBM. For Nb-4d at the interface of the heterostructures, the CBM has been upshifted most in Hetero1, which is even larger than the $NaNbO_3$. Figure 6k demonstrates that the upshifting of CBM is able to increases the shallow trap concentrations below CBM to enhance the ML performances. In $LiNbO_3$, O-s, p orbitals display one gap state within the bandgap. As shown in Figure 6l, with the concentration of Na^+ ions doping increases, such gap states not only shift but also split into two gap states in $NaNbO_3$. Such an evolution supports an efficient electron transfer from $LiNbO_3$ to $NaNbO_3$ via the interface of the heterostructure. Within in the heterostructure, the Li, Na and O states are significant contributions to the trap levels, which significantly promotes the deep and shallow trap distributions and concentrations. Therefore, the remarkable self-recoverable ML performances of LNNOP are attributed to the formation of local heterostructures, which not only increases the trap distributions but also promotes electron transfer efficiency. With the optimized electronic structures, the improved ML is realized in LN0.5.

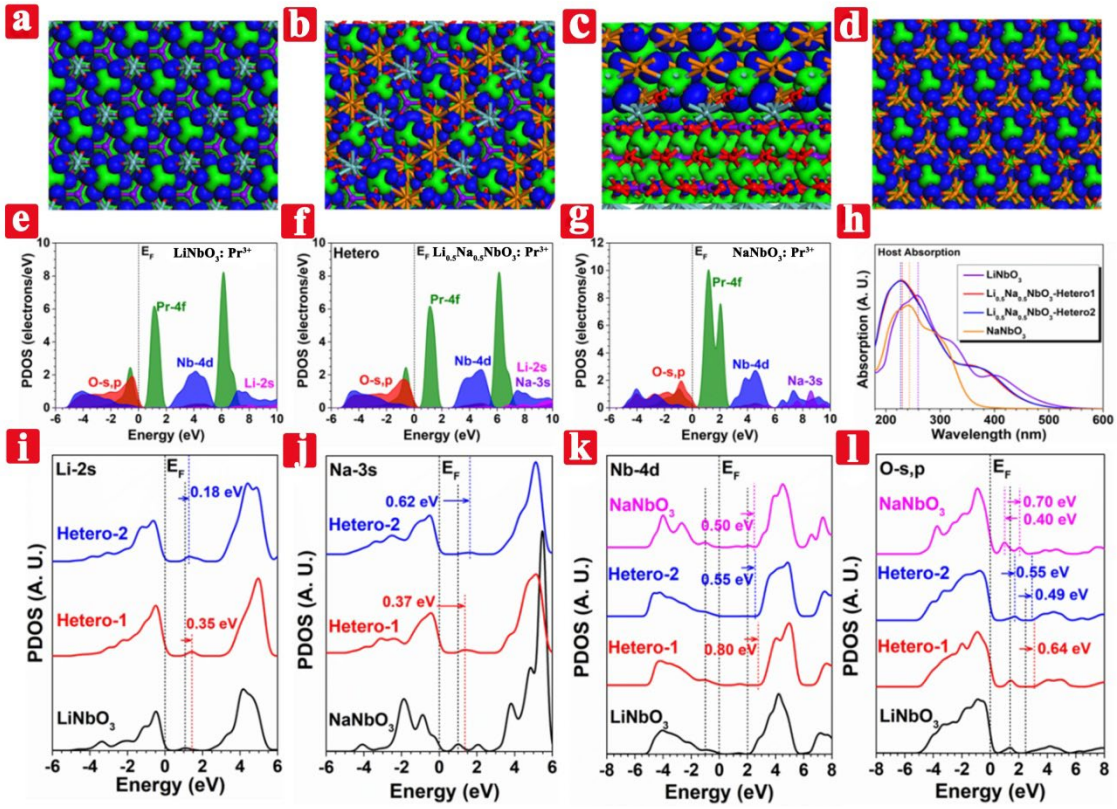

Figure 6. The 3D contour plot of electronic distributions of $LiNbO_3$ (a); LN0.5-Hetero1 (b); LN0.5-Hetero2 (c); and $NaNbO_3$ (d); Purple balls = Li, Orange balls = Na, Cyan balls = Nb and Red balls = O; the PDOS of $LiNbO_3$: Pr^{3+} (e); LN0.5-Hetero1 (f) and $NaNbO_3$: Pr^{3+} (g); the simulated absorption spectra of $LiNbO_3$, $Li_{0.5}Na_{0.5}NbO_3$-Hetero1, $Li_{0.5}Na_{0.5}NbO_3$-Hetero2 and $NaNbO_3$ (h); the band offset of different elements: (i) Li-2s, (j) Na-3s and (k) Nb-4d and (l) O-s, p.

3. Conclusion

In summary, a series of LNx ML materials have been developed, which modulated electronic structures and improved the ML performances by constructing heterostructures of the LNx system. XPS results confirm that the increases of Na^+ doping lead to the increased valence states of Nb. Especially, TL curves under sunlight irradiation for different times and ML peaks intensity under continuous compression for 10 cycles of LN0.5 confirm that the LN0.5 can be activated by sunlight to achieve high repeatable ML performance. The ML performance of LN0.5 is analyzed by exploring different sunlight irradiation times and pre-heating treatments. The result is unambiguously confirmed that the mechanical to the optical energy conversion process in LN0.5. Meanwhile, we proposed the appropriate mechanism model to explain the

ML mechanism of LN0.5, which proves that the LN0.5 relies on the trap structures and piezoelectricity coupling interaction to achieve its excellent ML performance. In addition, the DFT calculations have further confirmed that the Na^+ ions dopings enable more shallow and deep traps by modulating the electronic structures of $LiNbO_3$, especially the interface of the heterostructure. With broad trap distributions, the ML is further improved due to the promoted electron-hole recombination process. The investigation supplies a new strategy and method for the development of excellent ML materials with high repeatability and high brightness, which are also expected to promote the rapid application of ML materials for stress visualization.

4. Experimental section

Synthesis of $Li_{1-x}Na_xNbO_3$: Pr^{3+}. A series of $Li_{1-x}Na_xNbO_3$: Pr^{3+}(x=0, 0.2, 0.5, 0.8, 1.0) (LNx) samples were synthesized by high temperature solid-state method. Stoichiometry amounts of Li_2CO_3, Na_2CO_3, Nb_2O_5, Pr_6O_{11} were mixed in an agate mortar with ethanol. The doping concentration of Pr^{3+} was confirmed at 1%. After fully grinding, the mixtures were put into crucibles and calcined at 1150 °C for 6 h with a heating rate of 3 °C/min. After cooling to room temperature naturally, the as-obtained samples were grounded into powder for the following measurements.

Characterizations. The phase structure of the as-prepared powders was identified by X-ray diffraction (XRD) (XPert Pro X-ray diffractometer), using Cu Kα radiation. The data for phase identification were collected from 10° to 80° in a step size of 0.02°. The XRD data were refined by the Rietveld method using the general structure analysis system (GSAS) refinement program. The room temperature photoluminescence (PL) and photoluminescence excitation (PLE) were recorded by using a JASCO FP-8600 fluorescence spectrophotometer. To evaluate the ML properties, pellets with a diameter of 25 mm and a thickness of 15 mm were prepared by mixing LNx powder and optical epoxy resin. The pellets were exposed to sunlight at room temperature for 5 min, 30 min, 1 h, 3 h, 5 h, or exposed to UV light and blue LED for 5 min, respectively.

The ML intensity under a load (0-1000 N) was measured with a universal testing machine and a photon-counting system. ML photographs were recorded using a Nikon D5200 camera. ML spectra were recorded with a QE Pro photon multichannel analyzer system (Ocean Optics). The thermoluminescence (TL) curves were measured with a FJ-427A1 TL meter (Beijing Nuclear Instrument Factory, Beijing, China). The weight of the measured samples was constant (0.0020 g). Prior to the TL measurement, the samples were first exposed to the irradiation from sunlight (sunny day) for 5 min, 30 min, 1 h, 3 h, 5 h, respectively, then heated from 300 to 600 K with a rate of 1 K/s.

Calculation Setup. The DFT calculations within CASTEP packages are selected to investigate the electronics modulation induced by Na^+ ions doped in $LiNbO_3$.[39] The generalized gradient approximation (GGA) and Perdew-Burke-Ernzerhof (PBE) have been selected for the description of the exchange-correlation energy.[40-42] Meanwhile, we have set the 380 eV as the cutoff energy of the plane-wave basis with ultrafine quality. Based on the ultrasoft pseudopotentials, the Broyden-Fletcher-Goldfarb-Shannon (BFGS) algorithm and the coarse quality of k-points have been applied for the energy minimization.[43] The spin-polarizations have been applied for all the calculations, where the value of the total moment is determined by the sum of formal spins in the system. To accomplish the geometry optimizations, the convergence criteria are set as below: the Hellmann-Feynman forces on the atom should not exceed 0.001 eV/Å, the total energy difference should be less than 5×10^{-5} eV/atom, and the inter-ionic displacement should not exceed 0.005 Å.

Supporting Information

Supporting Information is available from the Wiley Online Library or from the author.

Acknowledgements

This work was partially supported by the Natural Science Foundation of China (11804255, 12074298, 21771156), the Natural Science Foundation of Jiangsu Province (BK20190212), the Early Career Scheme (ECS) fund (Grant No. PolyU 253026/16P) from the Research Grant Council (RGC) in Hong Kong and Grant-in-Aid for Scientific Research (KAKENHI) from Japan Society for the Promotion of Science (JSPS) Grant Number 19H00835, 17H06374.

References

[1] Wang X, Ling R, Zhang Y, et al. Oxygen-assisted preparation of mechanoluminescent ZnS: Mn for dynamic pressure mapping. *Nano Res*, 2018, 11(4): 1967-1976.

[2] Xu C N, Watanabe T, Akiyama M, et al. Artificial skin to sense mechanical stress by visible light emission. *Appl. Phys. Lett.*, 1999, 74(9): 1236-1238.

[3] Jeong S M, Song S, Seo H J, et al. Battery-free, human-motion-powered light-emitting fabric: mechanoluminescent textile. *Adv. Sustain. Syst.*, 2017, 1(12): 1700126.

[4] Zhuang Y, Tu D, Chen C, et al. Force-induced charge carrier storage: a new route for stress recording. *Light Sci. Appl.*, 2020, 9(1): 1-9.

[5] Zhang J C, Pan C, Zhu Y F, et al. Achieving thermo-mechano-opto-responsive bitemporal colorful luminescence via multiplexing of dual lanthanides in piezoelectric particles and its multidimensional anticounterfeiting. *Adv. Mater.*, 2018, 30(49): 1804644.

[6] Jeong S M, Song S, Lee S K, et al. Color manipulation of mechanoluminescence from stress-activated composite films. *Adv. Mater.*, 2013, 25(43): 6194-6200.

[7] Zhang H, Yamada H, Terasaki N, et al. Blue light emission from stress-activated $CaYAl_3O_7$: Eu. *J. Electrochem. Soc.*, 2008, 155(5): J128.

[8] Zhang H, Yamada H, Terasaki N, et al. Green mechanoluminescence of $Ca_2MgSi_2O_7$: Eu and $Ca_2MgSi_2O_7$: Eu, Dy. *J. Electrochem. Soc.*, 2007, 155(2): J55.

[9] Zhang J C, Wang X, Marriott G, et al. Trap-controlled mechanoluminescent materials. *Prog. Mater. Sci.*, 2019, 103: 678-742.

[10] Chen C, Zhuang Y, Tu D, et al. Creating visible-to-near-infrared mechanoluminescence in mixed-anion compounds $SrZn_2S_2O$ and SrZnSO. *Nano Energy*, 2020, 68: 104329.

[11] Xu C N, Watanabe T, Akiyama M, et al. Direct view of stress distribution in solid by mechanoluminescence. *Appl. Phys. Lett.*, 1999, 74(17): 2414-2416.

[12] Yamada H, Fu X, Xu C N. Enhancement of adhesion and triboluminescent properties of $SrAl_2O_4$: Eu^{2+} films fabricated by RF magnetron sputtering and postannealing techniques. *J.*

Electrochem. Soc., 2007, 154(11): J348.

[13] Xiong P, Huang B, Peng D, et al. Self-Recoverable Mechanically Induced Instant Luminescence from Cr^{3+}-Doped $LiGa_5O_8$. *Adv. Funct. Mater.*, 2021: 2010685.

[14] Chandra V K, Chandra B P, Jha P. Self-recovery of mechanoluminescence in ZnS: Cu and ZnS: Mn phosphors by trapping of drifting charge carriers. *Appl. Phys. Lett.*, 2013, 103(16): 161113.

[15] Pan C, Dong L, Zhu G, et al. High-resolution electroluminescent imaging of pressure distribution using a piezoelectric nanowire LED array. *Nat. Photonics*, 2013, 7(9): 752-758.

[16] Chandra B P, Baghel R N, Chandra V K. Mechanoluminescence glow curve of ZnS: Mn. *Chalcogenide Lett*, 2010, 7(1): 1-9.

[17] Chandra B P, Xu C N, Yamada H, et al. Luminescence induced by elastic deformation of ZnS: Mn nanoparticles. *J. Lumin.*, 2010, 130(3): 442-450.

[18] Peng D, Jiang Y, Huang B, et al. A ZnS/CaZnOS Heterojunction for Efficient Mechanical-to-Optical Energy Conversion by Conduction Band Offset. *Adv. Mater.*, 2020, 32(16): 1907747.

[19] Wang X, Zhang H, Yu R, et al. Dynamic pressure mapping of personalized handwriting by a flexible sensor matrix based on the mechanoluminescence process. *Adv. Mater.*, 2015, 27(14): 2324-2331.

[20] Moon Jeong S, Song S, Lee S K, et al. Mechanically driven light-generator with high durability. *Appl. Phys. Lett.*, 2013, 102(5): 051110.

[21] Xu C N, Yamada H, Wang X, et al. Strong elasticoluminescence from monoclinic-structure SrAl2O4. *Appl. Phys. Lett.*, 2004, 84(16): 3040-3042.

[22] Terasaki N, Xu C N, Li C, et al. Visualization of active crack on bridge in use by mechanoluminescent sensor[C]//Health Monitoring of Structural and Biological Systems 2012. International Society for Optics and Photonics, 2012, 8348: 83482D.

[23] Zhang J C, Long Y Z, Yan X, et al. Creating recoverable mechanoluminescence in

piezoelectric calcium niobates through Pr^{3+} doping. *Chem. Mater.*, 2016, 28(11): 4052-4057.

[24] Tu D, Xu C N, Yoshida A, et al. $LiNbO_3$: Pr^{3+}: a multipiezo material with simultaneous piezoelectricity and sensitive piezoluminescence. *Adv. Mater.*, 2017, 29(22): 1606914.

[25] Tu D, Xu C N, Kamimura S, et al. Ferroelectric $Sr_3Sn_2O_7$: Nd^{3+}: A New Multipiezo Material with Ultrasensitive and Sustainable Near-Infrared Piezoluminescence. *Adv. Mater.*, 2020, 32(25): 1908083.

[26] Pan Z, Lu Y Y, Liu F. Sunlight-activated long-persistent luminescence in the near-infrared from Cr^{3+}-doped zinc gallogermanates. *Nat. Mater.*, 2012, 11(1): 58-63.

[27] Wang P, Xu X, Zhou D, et al. Sunlight activated long-lasting luminescence from $Ba_5Si_8O_{21}$: Eu^{2+}, Dy^{3+} phosphor. *Inorg. Chem*., 2015, 54(4): 1690-1697.

[28] Zhou Z, Wang X, Yi X, et al. Rechargeable and sunlight-activated $Sr_3Y_2Ge_3O_{12}$: Bi^{3+} UV-Visible-NIR persistent luminescence material for night-vision signage and optical information storage. *Chem. Eng. J.*, 2020: 127820.

[29] Hara H, XU C N, Wang R, et al. Control of crystal structure and performance evaluation of multi-piezo material of $Li_{1-x}Na_xNbO_3$: Pr^{3+}. *J. Ceram. Soc. Jpn.*, 2020, 128(8): 518-522.

[30] Peel M D, Ashbrook S E, Lightfoot P. Unusual Phase Behavior in the Piezoelectric Perovskite System, $Li_xNa_{1-x}NbO_3$. *Inorg. Chem*., 2013, 52(15): 8872-8880.

[31] Dixon C A L, Lightfoot P. Complex octahedral tilt phases in the ferroelectric perovskite system $Li_xNa_{1-x}NbO_3$. *Phys. Rev. B*, 2018, 97(22): 224105.

[32] Duan P, Chen Z, Dai S, et al. $La_{0.7}Pr_{0.3}MnO_3$ ceramic: An electron-doped colossal magnetoresistive manganite. *Appl. Phys. Lett.*, 2004, 84(23): 4741-4743.

[33] Sang J, Zhou J, Zhang J, et al. Multilevel Static-Dynamic Anticounterfeiting Based on Stimuli-Responsive Luminescence in a Niobate Structure. *ACS Appl. Mater. Interfaces*, 2019, 11(22): 20150-20156.

[34] Skryleva E A, Kubasov I V, Kiryukhantsev-Korneev P V, et al. XPS study of Li/Nb ratio in $LiNbO_3$ crystals. Effect of polarity and mechanical processing on $LiNbO_3$ surface chemical

composition. *Appl. Surf. Sci.*, 2016, 389: 387-394.

[35] Lazarowska A, Mahlik S, Marek G, et al. High pressure luminescence and time resolved spectra of $LiNbO_3$: Pr^{3+}. *Photonics. Lett. Pol.*, 2011, 3(2): 67-69.

[36] Kortüm G, Braun W, Herzog G. Principles and techniques of diffuse-reflectance spectroscopy. *Angew. Chem., Int. Ed*, 1963, 2(7): 333-341.

[37] Zhuang Y, Xie R J. Mechanoluminescence Rebrightening the Prospects of Stress Sensing: A Review. *Adv. Mater.*, 2021: 2005925.

[38] Chen B, Zhang X, Wang F. Expanding the Toolbox of Inorganic Mechanoluminescence Materials. Accounts of Materials Research, 2021.

[39] S. J. Clark; M. D. Segall; C. J. Pickard; P. J. Hasnip; M. J. Probert; K. Refson; M. C. Payne, First Principles Methods Using Castep. *Z. Kristallogr.-Cryst. Mater.* 2005, 220 (5-6), 567-570.

[40] Perdew J P, Burke K, Ernzerhof M. Generalized gradient approximation made simple. *Phys. Rev. Lett.*, 1996, 77(18): 3865.

[41] Hasnip P J, Pickard C J. Electronic energy minimisation with ultrasoft pseudopotentials. *Comput. Phys. Commun.*, 2006, 174(1): 24-29.

[42] Perdew J P, Chevary J A, Vosko S H, et al. Atoms, molecules, solids, and surfaces: Applications of the generalized gradient approximation for exchange and correlation. *Phys. Rev. B* 1992, 46 (11), 6671.

[43] Head J D, Zerner M C. A Broyden-Fletcher-Goldfarb-Shanno optimization procedure for molecular geometries. *Chem. Phys. Lett.*, 1985, 122(3): 264-270.